H^+-H_2O collisions studied by time-dependent density-functional theory combined with the molecular dynamics method

Xuhai Hong,[1] Feng Wang,[2] Yong Wu,[1,*] Bingcong Gou,[2] and Jianguo Wang[1,†]
[1]*Institute of Applied Physics and Computational Mathematics, Beijing 100088, China*
[2]*School of Physics, Key Laboratory of Cluster Science of Ministry of Education, Beijing Institute of Technology, Beijing 100081, China*
(Received 23 December 2015; published 15 June 2016)

H^+-H_2O collisions are investigated using the time-dependent density-functional theory combined with the molecular dynamics method, in which the electrons are described quantum mechanically within the framework of time-dependent density-functional theory and the ionic cores are described classically by Newton's equations. The feedback between quantum electrons and classical ions is self-consistently coupled by Ehrenfest's method. The electron capture, electron loss, and ionization cross sections are obtained in the energy range of 1–1000 keV and excellent agreements are achieved with available experimental and theoretical data. The orientation effects of the H_2O target are found to be significant in the collision processes, especially in low-energy collisions.

DOI: 10.1103/PhysRevA.93.062706

I. INTRODUCTION

Abundant collisions between ions and atoms or molecules exist in the laboratory and astrophysical plasma environments, where the electron density and temperature are usually relatively low [1]. And the collisions between ions and atoms or molecules play an important role in the particle evolution and energy transformation of the plasma. Ion-atom collisions have been studied more extensively and been better understood in recent decades. For ion-molecule collisions, although significant progress has been made in theoretical studies in recent years, the elaborate treatment of ion-molecule collisions is still a challenging task due to the complicated dynamics and physics effects evolved in the collisions. For example, multielectron correlation effects and multichannel and multibody coupling effects become significant, especially in low- and intermediate-energy collisions.

Concerning H^+-H_2O collisions, they have extensive applications in both astrophysics and biological physics studies. It is well known that the atmosphere of planets and comets consists of N_2, O_2, H_2, H_2O, CO, CO_2, CH_4, etc., and these neutral species frequently collide with high-speed solar wind ions, including H^+, He^{2+}, and other minor ions, and solar wind ion x rays are emitted. Therefore, investigation of the collision processes between these solar wind ions and neutral molecules are important in the interpretation of solar wind x-ray emissions and solar wind particle reduction in cometary atmospheres [2]. In the study of biological physics, collisions of water molecules with protons have also received intensive attention, since the water molecule is the basic component of biological tissues. In radiobiology studies, it has been found that radiated water molecules usually produce large numbers of secondary low-energy electrons, ions, and radicals, and these particles cause indirect and direct biological damages to DNA molecules through a series of chain reactions [3].

Because of its importance in astrophysics and biological physics studies, collisions of $H^+ + H_2O$ have been studied extensively in both experiments and theories. Experimentally, a large number of measurements have been performed for proton-water collisions in past decades [4–14]. Measurements of electron capture and electron loss cross sections for protons in H_2O have been reported by Toburen *et al.* in the energy range of 100–2500 keV [5]. Electron capture cross sections have been measured by Berkner *et al.* using slow-ion collection technique in the energy range of 50–250 keV [6]. Total cross sections of electron capture and electron loss have been measured by Dagnac *et al.* for energies of 2–60 keV [7]. Cross sections for production of electrons and positive ions by proton impact on water vapor have been measured by Rudd *et al.* for energies of 7–4000 keV using the transverse-field method [8]. Absolute cross sections for electron ionization by protons of 15- to 150-keV energy have been measured by Bolorizadeh *et al.* [9]. Multiple ionization and fragmentation of H_2O by fast H^+ ions were studied by Werner *et al.* using a position- and time-sensitive multiparticle detector [10]. Measurements of the absolute integral cross sections for electron capture of 0.5-, 1.5-, and 5-keV protons by H_2O have been reported by Lindsay *et al.* [11]. Absolute measurements have been made of cross sections of single-electron capture in the energy range of 0.3–7.5 keV by Greenwood *et al.* [12]. Cross sections of ionization and electron capture have been measured by Gobet *et al.* using crossed-beam technique in collisions of water with 20- to 150-keV protons [13]. The electron capture and ionization cross sections of water during collisions with 15- to 3500-keV protons have been measured by Luna *et al.* using time-of-flight-based mass analysis [14].

Theoretically, various methods and models have been developed to treat proton-molecule collisions. Generally, there are four types of methods: the classical method, semiclassical method, perturbative approximation method, and quantum method. For intermediate- and high-energy collisions, the classical, semiclassical, and perturbative approximation methods work well. The three classical trajectory Monte Carlo (CTMC) models of Errea *et al.* [15], Abbas *et al.* [16], and Illescas *et al.* [17], the continuum distorted-wave (CDW) approximation of Gervais *et al.* [18], the basis generation method (BGM) of Lüdde *et al.* [19] and Murakami *et al.* [20], and the perturbative first Born (FB) approximation of Boudrioua *et al.* [21] have been applied to the study of H^+-H_2O collisions, and reliable results have been obtained for energies

*wu_yong@iapcm.ac.cn
†wang_jianguo@iapcm.ac.cn

higher than 20 keV. It should be noted that the results calculated by Murakami *et al.* [20] cover the large energy range of 20–700 keV. For low-energy collisions, quantum methods become more appropriate. The molecular orbital close-coupling (MOCC) approach of Mada *et al.* [22] has been applied to treat low-energy H^+- H_2O collisions for the energy range of 0.02–10 keV. The molecular-orbital (MO) based method of Gabàs *et al.* [23] has been applied to the study of H^+-H_2O collisions for the energy range of 1–40 keV. Their calculated results have obtained a good agreement with available experimental data. One may find that the above theoretical methods and models are not suitable for treating H^+-H_2O collisions in a wide range of collision energies.

In the present paper, the technique of time-dependent density-functional theory combined with the molecular dynamics method has been extended to treat H^+-H_2O collisions; it has been applied to treat ion-atom collisions successfully [24,25]. The electron capture, electron loss, and ionization cross sections are calculated over a wide energy range, from 1 to 1000 keV, and compared with available experimental and theoretical data. The dependence of the probabilities on the orientation of the water molecule has been well discussed. This paper is organized as follows. In Sec. II, we introduce the theoretical framework, emphasizing the description of features of the ion-molecule collision method. Section III reports the results and discussion, and a summary is given in Sec. IV. Atomic units (a.u.) are used throughout this paper unless otherwise specified.

II. THEORY

Time-dependent density-functional theory (TDDFT) can be viewed as an exact reformulation of the time-dependent many-body Schrödinger equation [26]. The key approximation made in practical applications is the approximation for the exchange-correlation (xc) potential. The foundation of modern TDDFT was laid by Runge and Gross [27], whose actual original motivation was the time-dependent description of scattering experiments. For an N-electron quantum system, a set of time-dependent Kohn-Sham (KS) equations subjected to an effective external potential $V_{\rm KS}$ is described by

$$i\frac{\partial}{\partial t}\phi_{i\sigma}(\mathbf{r},t)=\left[-\frac{\nabla^2}{2}+V_{\rm KS}[n](\mathbf{r},t)\right]\phi_{i\sigma}(\mathbf{r},t). \tag{1}$$

The kinetic operator is approximated in a real-space formulation by a high-order finite difference formula with nine points for each direction [28]. The Kohn-Sham orbitals (KSOs) $\phi_{i\sigma}(\mathbf{r},t)$ $(i=1,\ldots,N)$ are no longer the fundamental information carrier, as in conventional wave-function theory, but physically meaningless auxiliary quantities. Actually the time-dependent one-particle density of the system can be readily calculated from the KSOs:

$$n(\mathbf{r},t)=\sum_{\sigma=\uparrow\downarrow}\sum_{i}|\phi_{i\sigma}(\mathbf{r},t)|^2. \tag{2}$$

The effective external potential $V_{\rm KS}$ in Eq. (1) is decomposed into the external potential, Hartree potential, and xc potential

$$V_{\rm KS}[n](\mathbf{r},t)=V_{\rm ext}(\mathbf{r},t)+V_{\rm Hartree}[n](\mathbf{r},t)+V_{{\rm xc}\sigma}[n](\mathbf{r},t). \tag{3}$$

The first term is normally the Coulomb interaction between the active electrons and the ionic cores, which is described properly by norm-conserving pseudopotentials [29].

The next item is the electrostatic interaction between the electrons,

$$V_{\rm Hartree}(\mathbf{r},t)=\int d^3r'\frac{n(\mathbf{r},t)}{|\mathbf{r}-\mathbf{r}'|}. \tag{4}$$

In principle, the third term, the xc potential, should include all nontrivial many-body interactions and is nonlocally (in space and in time) dependent on the one-body density. However, the xc potential has not been accurately formulated so far, so it has to be approximated in practice. As a simple approximation to the $V_{{\rm xc}\sigma}$, the local density approximation (LDA) [30–32] based on the xc energy density of the homogeneous electron gas is used in our calculations:

$$V_{\rm xc}^{\rm LDA}[n](\mathbf{r})=\left.\frac{\partial\varepsilon_{\rm xc}^{\rm hom}[n]}{\partial n}\right|_{n=n(r,t)}. \tag{5}$$

Note that the accuracy of the calculated results is limited by the LDA applied in the present TDDFT calculation. The nonlocal part of the exchange correlation is not described well and highly excited states cannot be well treated in the present work. So far, the LDA has been applied successfully to a number of collision systems and gives satisfactory electron capture and electron loss cross sections [24,25,33–36].

The KSOs are propagated through the enforced time-reversal-symmetry method [37]:

$$\phi_{i\sigma}(\mathbf{r},t+\Delta t)=e^{-i\frac{\Delta t}{2}\hat{H}_{\rm KS}(t+\Delta t)}e^{-i\frac{\Delta t}{2}\hat{H}_{\rm KS}(t)}\phi_{i\sigma}(\mathbf{r},t). \tag{6}$$

Naturally, very slow and close collisions by an incident ion would trigger notable motion of ionic cores. The motion of ionic cores is described by classical Newton's equations,

$$M_\alpha\frac{\partial^2\mathbf{R}_\alpha}{\partial^2 t}=\mathbf{F}_\alpha, \tag{7}$$

where M_α and $\mathbf{R}_\alpha(t)$ are the mass and the coordinate of the ionic core labeled α. $\mathbf{F}_\alpha$, the classical electrostatic force of ionic core α, is exerted by other ionic cores and electrons.

In the semiclassical description of electron-ion dynamical evolution, the classical motion of ionic cores disturbs the time-dependent electronic density and the quantum electron density changes alter the forces acting on the classical ionic cores in turn. Therefore an appropriate coupling scheme is required to deal with quantum-classical feedback. Ehrenfest's method [38] is employed here to treat the feedback of electrons by applying an effective force on the classical ionic cores, which is given as the expectation value of the position R derivative of the effective external potential $V_{\rm KS}$. It has turned out to be quite reliable for the collisions of energetic ions [39].

The force $\mathbf{F}_\alpha$ exerted on the ionic cores labeled α is given by

$$\mathbf{F}_\alpha(t)=-\nabla_\alpha\sum_{\beta\neq\alpha}\frac{Z_\alpha Z_\beta}{|R_\alpha(t)-R_\beta(t)|}+\int_V d^3r n(\mathbf{r},t)\nabla_\alpha\sum_\alpha\frac{Z_\alpha}{|\mathbf{R}_\alpha(t)-\mathbf{r}|}. \tag{8}$$

Z_α is the charge of the ionic core labeled α. The first part of the force is produced by other ionic cores, and the second part is produced by electron density variation.

The Newton's equations in Eq. (7) are propagated through the velocity Verlet algorithm [40]:

$$\mathbf{R}_\alpha(t+\Delta t) = \mathbf{R}_\alpha(t) + \frac{\partial \mathbf{R}_\alpha}{\partial t}\Delta t + \frac{\mathbf{F}_\alpha(t)}{2M_j}\Delta t^2; \tag{9a}$$

$$\frac{\partial \mathbf{R}_\alpha(t+\Delta t)}{\partial t} = \frac{\partial \mathbf{R}_\alpha(t)}{\partial t} + \frac{\mathbf{F}_\alpha(t)+\mathbf{F}_\alpha(t+\Delta t)}{2M_j}\Delta t. \tag{9b}$$

At high impact energies, the present model can be simplified and the ionic cores comprising the water molecule can probably be regarded as fixed.

In the present H^+-H_2O collision, the two $1s$ electrons of the oxygen atom are assumed to be tightly bound to the nucleus, and they are described by an inert core, leaving eight active electrons in the water molecule. The eight spin-polarized KSOs are populated by active electrons with occupation numbers $n_{i\sigma} = 1, 1, 1, 1$. As the incident ion approaches the target molecule, the electron capture and electron loss processes are focused on

$$H^+ + H_2O \rightarrow H^n + \cdots, \tag{10a}$$

$$H^+ + H_2O \rightarrow (H_2O)^{m+} + \cdots. \tag{10b}$$

where n and m are the charge state of the incident ion and the target, respectively, after collision. The corresponding cross sections are obtained by integration over a series of impact parameters b,

$$\sigma_{1n}^{\rm cap} = 2\pi \int P_{1n}^{\rm cap}(b) b db, \tag{11a}$$

$$\sigma_{0m}^{\rm loss} = 2\pi \int P_{0m}^{\rm loss}(b) b db, \tag{11b}$$

where $P_{1n}^{\rm cap}(b)$ and $P_{0m}^{\rm loss}(b)$ are the stationary probabilities of the incident ion's capturing $1-n$ and the target molecule's losing $m-0$ electrons at the end of collisions, respectively.

The corresponding total cross sections are calculated by summing over the above cross sections,

$$\sigma_{\rm total}^{\rm cap} = \sum_{n=-1}^{0} (1-n)\sigma_{1n}^{\rm cap}, \tag{12a}$$

$$\sigma_{\rm total}^{\rm loss} = \sum_{m=0}^{8} m\sigma_{0m}^{\rm loss}, \tag{12b}$$

and the total ionization cross sections are obtained by subtracting the electron capture cross section from the electron loss cross section,

$$\sigma_{\rm total}^{\rm ion} = \sigma_{\rm total}^{\rm loss} - \sigma_{\rm total}^{\rm cap}. \tag{13}$$

It should be noted that the present treatment of ionization is a simple approximation, which cannot distinguish the transfer ionization from the total ionization processes. And another limitation is that large calculation uncertainties will arise when the electron capture and electron loss cross sections are close to each other [41–43].

The stationary probabilities $P_{1n}^{\rm cap}(b)$ and $P_{0m}^{\rm loss}(b)$ in Eqs. (11a) and (11b) are extracted using the method developed by Lüdde and Dreizler, which has been proven successful in treating many-electron collision systems [44]. We give brief definitions of $P_{1n}^{\rm cap}$ and $P_{0m}^{\rm loss}$ below.

The Slater determinant Φ, constructed by a set of KSOs as the zeroth-order approximation to the total wave function of the system, is expressed as

$$\Phi = \frac{1}{\sqrt{8!}} \det|\phi_1 \ldots \phi_8|. \tag{14}$$

The overlap integrals of Slater determinants can be obtained [44] as

$$\langle\Phi|\Phi\rangle_{\tau_1\ldots\tau_8}^{k} = \frac{1}{\binom{8}{k}} \sum_{\tau_1\ldots\tau_8} \begin{vmatrix} \langle\phi_1|\phi_1\rangle_{\tau_1} & \cdots & \langle\phi_1|\phi_8\rangle_{\tau_1} \\ \vdots & \vdots & \vdots \\ \langle\phi_8|\phi_1\rangle_{\tau_8} & \cdots & \langle\phi_8|\phi_8\rangle_{\tau_8} \end{vmatrix}, \tag{15}$$

where $k = 1-n$ for the electron capture process and $k = 8-m$ for the electron loss process. In our real-space simulations, two regions are defined: one is the bound region $\mathbb{A}$ (our simulation box) surrounding the incident ion or target; the other is the complementary region $\mathbb{B}$. The symbol $\tau_1 \ldots \tau_8$ denotes all possible region permutations without repetition. Each region permutation gives a possible position state of all electrons in full space where $1-n$ (for the electron capture process) or $8-m$ (for the electron loss process) electrons are bound in region $\mathbb{A}$ and the other electron is in region $\mathbb{B}$.

The stationary probabilities $P_{1n}^{\rm cap}$ and $P_{0m}^{\rm loss}$ are identified by

$$P_{1n}^{\rm cap} = \binom{8}{1-n} \langle\Phi|\Phi\rangle_{\tau_1\ldots\tau_8}^{1-n}, \tag{16a}$$

$$P_{0m}^{\rm loss} = \binom{8}{8-m} \langle\Phi|\Phi\rangle_{\tau_1\ldots\tau_8}^{8-m}, \tag{16b}$$

where the binomial coefficient stems from the fact that all integrals for a given $1-n$ or $8-m$ give the same contribution.

In order to have an affordable calculation cost, it is necessary to use finite real-space grids in collision dynamics simulations. During the collision, an incident ion with a certain velocity approaches the target atom or molecule. After the incident ion captures electrons, it is scattered out of the simulation box. Therefore the electron capture information on the incident ion cannot be observed within finite real-space grids. The key problem is the rearrangement between incident ion and target after collisions. This problem can be solved reasonably by the proposed coordinate space translation technique [24], which provides a flexible choice to translate the incident ion or the target within the simulation box (region $\mathbb{A}$) and scatter the other one out of the simulation box by the translational transforms in both momentum and coordinate. Coordinate space translation has been applied successfully to study the electron capture process in several ion-atom collision systems and gives satisfactory results [25]. The entire collision dynamical evolution is carried out in the real-space, real-time package Octopus [45].

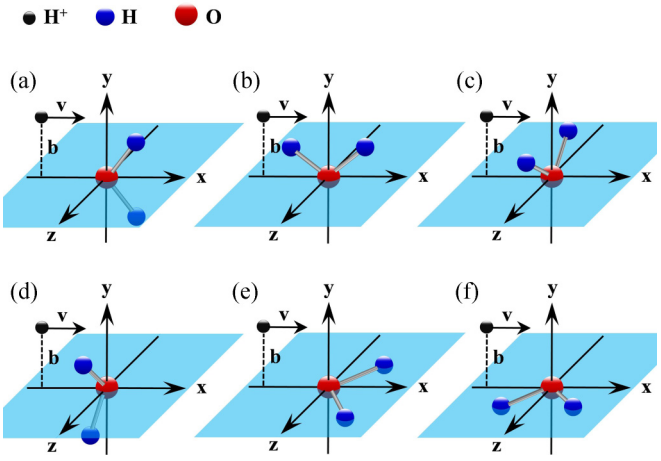

FIG. 1. Geometrical diagrams of collisions between protons and water molecules. The proton, hydrogen atom, and oxygen atom are represented by different-sized circles. Water molecules are located (a), (b) in the xy half-plane with $x > 0$ and $y > 0$, (c), (d) in the yz half-plane with $y > 0$ and $z > 0$, and (e), (f) in the xz half-plane with $x > 0$ and $z > 0$. The velocity vector $\mathbf{v}$ of the incident proton is oriented along the x direction. The impact parameter b is oriented along the y direction.

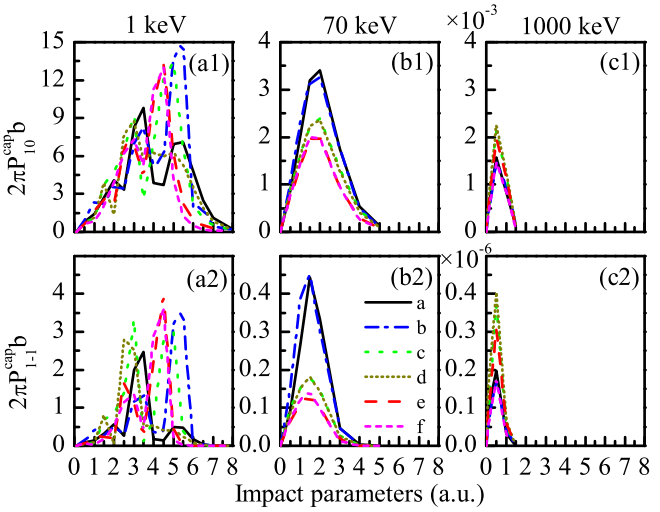

FIG. 2. Electron capture probabilities ($2\pi P_{1n}^{\text{cap}} b$; $n = 0$ and -1 represent single- and double-electron capture, respectively) as a function of the impact parameters at an incident energy of 1, 70, and 1000 keV, respectively. The probabilities under the collision configurations in Figs. 1(a)–1(f) are indicated by different lines.

III. RESULTS AND DISCUSSION

In the present calculations, six representative configurations are selected in simulating H^+-H_2O collisions and the cross sections for each configuration are calculated; these are then averaged to obtained the orientation-averaged cross sections to compare with the experimental data, since the incident proton collides with the water molecule at random orientations in measurements. As shown in Fig. 1, six representative configurations for a water molecule colliding with a proton are presented. In the present real-space calculations, the bound region $\mathbb{A}$ is a sphere simulation box of radius 25 a.u. In order to absorb the ionized electrons in a smooth way with no unfavorable reflection, an absorbing potential [46–50] with a thickness of $R_0 = 5$ a.u. (in the range of 20–25 a.u.) is located at the boundary layer of the real-space sphere simulation box. The specific form of the absorbing potential is

$$V_{\text{abs}} = \begin{cases} V_0 \sin^2\left(\frac{r-R_0}{R-R_0}\frac{\pi}{2}\right), & R_0 < r \leqslant R, \\ 0, & 0 < r \leqslant R_0, \end{cases} \tag{17}$$

where $V_0 = 2$ a.u. represents the height of the imaginary potential. In order to ensure convergence and stabilization of the evolution processes, the steps of coordinate grids and the evolution time are optimized. A time step of 0.025 a.u. is used, and the grid step decreases with an increase in the incident energy: a grid step of 0.33 a.u. for incident energies less than 100 keV, a grid step of 0.25 a.u. for incident energies of 200–600 keV, and a 0.2-a.u. step for incident energies higher than 800 keV. At the beginning of our simulation, the incident ion H^+ is placed at $\mathbf{R}_{H^+} = (-15, b, 0)$, where b is the impact parameter, and the oxygen atom of the water molecule is placed at the original point in the simulation box. The spin-polarized KSOs of H_2O for each orientation are obtained by standard density-functional theory. Then the incident proton passes by the H_2O target along the x direction, and electrons and ions are propagated based on the time-dependent KS equations and Ehrenfest's method. At the end of evolution when the incident proton and the target molecule are separated by a distance of 40 a.u., the coordinate space translation technique is applied and the incident proton or target molecule is moved to the center of the simulation box. Then a further evolution is performed to get rid of the residual ionized electrons to obtain the convergent stationary probabilities. In the time-dependent simulation of ion-atom and ion-molecule collisions, the selections of the simulation box size and the starting and ending points of the incident ions will affect the scattering cross sections obtained [51] and the convergence of these parameters have to be checked. In the present calculations, negligible effects have been found in the energy range considered and the discrepancies of cross-section results are less than 1.4%, when the simulation box sizes were changed from 25 to 35 a.u., the starting point of the proton from 15 to 30 a.u., and the ending distance from 40 to 60 a.u.

A. Electron capture

In Fig. 2, single- and double-electron capture probabilities $2\pi P_{1n}^{\text{cap}} b$ ($n = 0, -1$) are presented for three typical incident energies: 1, 70, and 1000 keV. It is found that with increasing impact energy, the capture probabilities tend to converge at a smaller impact parameter rapidly, which indicates that close collisions become important for higher energy collisions. And the electron capture probabilities converge well as the impact parameter is increased to 8, 5, and 1.5 a.u. for the three energies, respectively. From low to high impact energy, the electron capture probabilities for the collision configurations in Figs. 1(a)–1(f) show large differences. At the low incident energy of 1 keV, the probability lines become divergent for all six collision configurations, which indicates that low-energy collisions are more sensitive to the distribution of an electron

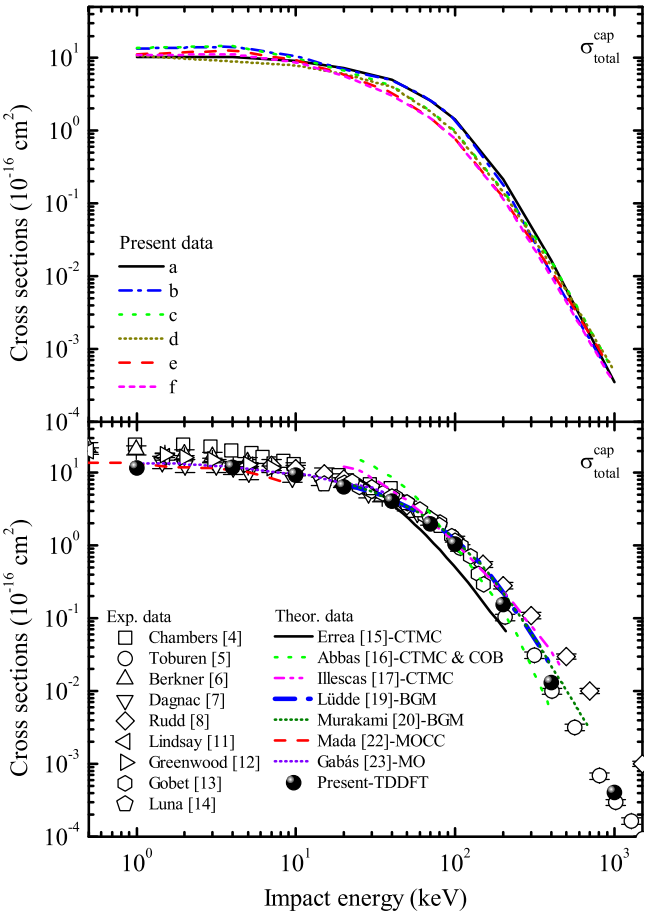

FIG. 3. Top: Present cross sections of electron capture under the collision configurations in Figs. 1(a)– 1(f). Bottom: Present total cross sections of electron capture ($\sigma_{\text{total}}^{\text{cap}}$; filled circles) as a function of the incident energies. Other theories, lines; experiments, open symbols.

cloud. At the intermediate incident energy of 70 keV, the six probability lines present three groups, namely, Figs. 1(a)–1(f), for water molecules located in the xy plane, yz plane, and xz plane, respectively. For the high incident energy of 1000 keV, the probability curves for different collision configurations become more convergent and the double-electron capture processes become negligible, about four orders lower than the single-electron capture probability in magnitude.

By integration on the electron capture probabilities, the total electron capture cross sections $\sigma_{\text{total}}^{\text{cap}}$ are calculated in the energy range of 1–1000 keV through Eqs. (11a) and (12a). In Fig. 3, the present total cross sections of electron capture are compared with the experimental [4–8,11–14] and theoretical [15–17,19,20,22,23] data available. It is found that the total electron capture cross sections decrease with an increase in the impact energy. Generally, there are good agreements between the present calculations and the available data except at very low and very high impact energies. At the lowest energy considered, 1 keV, the present calculations agree well with the molecular-orbital close-coupling (MOCC) result of Mada *et al.* [22] and the molecular-orbital (MO) data of Gabàs *et al.* [23] but are about 50% lower than the older measurements by Chambers [4] and Berkner [6]. This discrepancy is mainly due to insufficient consideration of the electron correlation effect described by the LDA in the present calculation, since the electron correlation effect becomes more important in low-energy collisions. As Belkić *et al.* [41–43] found that electron correlation effects are important in ion-atom collisions over a wide energy range, which are not negligible even at high energies. For energies higher than 200 keV, the present calculations agree well with the calculations of Abbas *et al.* [16], Lüdde *et al.* [19], and Murakami *et al.* [20] and the measurements by Toburen *et al.* [5] but are about 50% lower than the newer measurements by Rudd *et al.* [8] and the latest calculations of Illescas *et al.* [17]. In the measurements by Rudd *et al.*, the electron capture cross sections are obtained by subtracting the electron ionization cross sections from the loss cross sections. These two quantities are near the same in value and the subtraction is obtained with a large uncertainty, which partially explains the divergence of the measurements by Rudd *et al.* Meanwhile, in the range of intermediate incident energy, the calculations of Abbas *et al.* [16] and Illescas *et al.* [17] obviously overestimate the experimental data, which is mainly caused by the simple classical descriptions of the target molecule. Moreover, BGM calculations were performed by Lüdde *et al.* [19] in the energy range 20–500 keV and Murakami *et al.* [20] in the energy range 20–700 keV, and they obtained results consistent with the experiments due to the quantal treatment of the electrons.

B. Electron loss and ionization

The probabilities of single-, double-, three-, and four-electron loss $2\pi P_{0m}^{\text{loss}} b$ $(n = 1, 2, 3, 4)$ are shown in Fig. 4. It can be observed that the electron loss probabilities decrease rapidly as the electron loss number increases, and the probabilities become negligible for electron loss numbers larger than four and are not presented in Fig. 4 for clarity. With increasing electron loss number, the electron loss probabilities prefer to populate at smaller impact parameters, which indicates that multielectron processes tend to occur in close collisions. A notable phenomenon can be observed: the electrons in the water target are easily lost, while the proton impacts the water target within the molecule plane, namely, the configuration shown in Fig. 1(b). It can be qualitatively explained that the incident proton would go through a denser electron cloud and remove more electrons during the collision configuration in Fig. 1(b). Another notable phenomenon is that electron loss processes tend to occur in close collisions with an increasing electron loss number, but independent of the impact energy, as shown in Fig. 4, which is distinct from the feature of the electron capture process shown in Fig. 2. Comparing Figs. 2 and 4, it is found that the electron capture process preferably occurs in low-energy collisions, whereas the electron ionization process preferably occurs at higher incident energies. Moreover, the electron ionization process can take place at longer distances.

By integration of the electron loss probabilities, the cross sections for single-, double-, three-, and four-electron loss $\sigma_{0m}^{\text{loss}}$ $(m = 1, 2, 3, 4)$ are calculated in the energy range 1–1000 keV using Eq. (11b). In Fig. 5, the present calculations are compared with the only BGM calculations of Murakami *et al.* [20]. It is found that there is excellent agreement

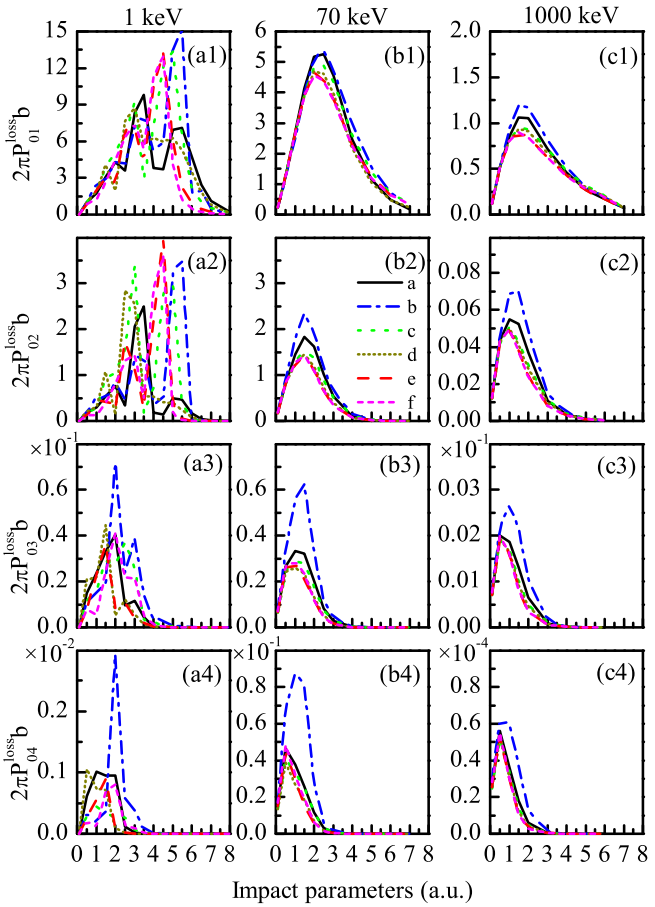

FIG. 4. Electron loss probabilities ($2\pi P_{0m}^{\rm loss} b$; $m = 1$, 2, 3, and 4 correspond to single-, double-, three-, and four-electron loss) as a function of the impact parameters at an incident energy of 1, 70, and 1000 keV, respectively. Probabilities under the collision configurations in Figs. 1(a)–1(f) are indicated by different lines. Probabilities of the loss of more than four electrons are extremely low and not shown for the sake of clarity.

between the present results and the BGM calculations of $\sigma_{0m}^{\rm loss}$ ($m = 1$, 2, 3), and the electron loss cross sections present a different tendency with an increase in the electron loss number and the collision energy. With increasing electron loss number, the electron loss cross sections decrease one to two orders in magnitude. For the single- and double-electron loss processes, the cross sections decrease slowly with an increase in the incident energy, but $\sigma_{03}^{\rm loss}$ and $\sigma_{04}^{\rm loss}$ exhibit an obvious maximum at an incident energy of around 40 keV. As far as we know, no other data are available for the four-electron loss cross section $\sigma_{04}^{\rm loss}$ up to now. New studies, especially measurements, are expected to determine the accuracy of the present calculations.

The total electron loss cross sections $\sigma_{\rm total}^{\rm loss}$ are calculated by Eq. (12b) and compared with available experimental data [8,10,13,14] and theoretical data [20], as shown in Fig. 6. Generally, there is good agreement between the present calculations and the available measurements [8,10,13,14], except for energies higher than 400 keV. The only available theoretical data of Murakami *et al.* [20] are calculated based on the BGM in the energy range 20 to 5000 keV, which agree

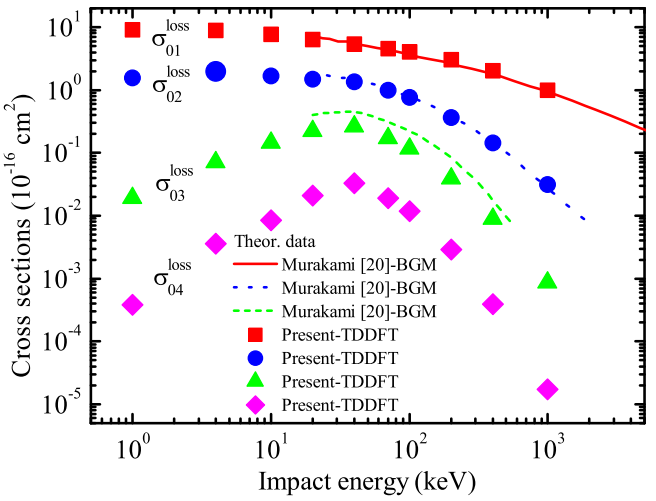

FIG. 5. Present electron loss cross sections ($\sigma_{0m}^{\rm loss}$; $m = 1$, 2, 3, and 4 correspond to single-, double-, three-, and four-electron loss, indicated by filled squares, circles, upward triangles, and diamonds) as a function of the incident energies. The electron loss cross sections for more than four electrons are extremely small and not shown for the sake of clarity. Other theory, lines.

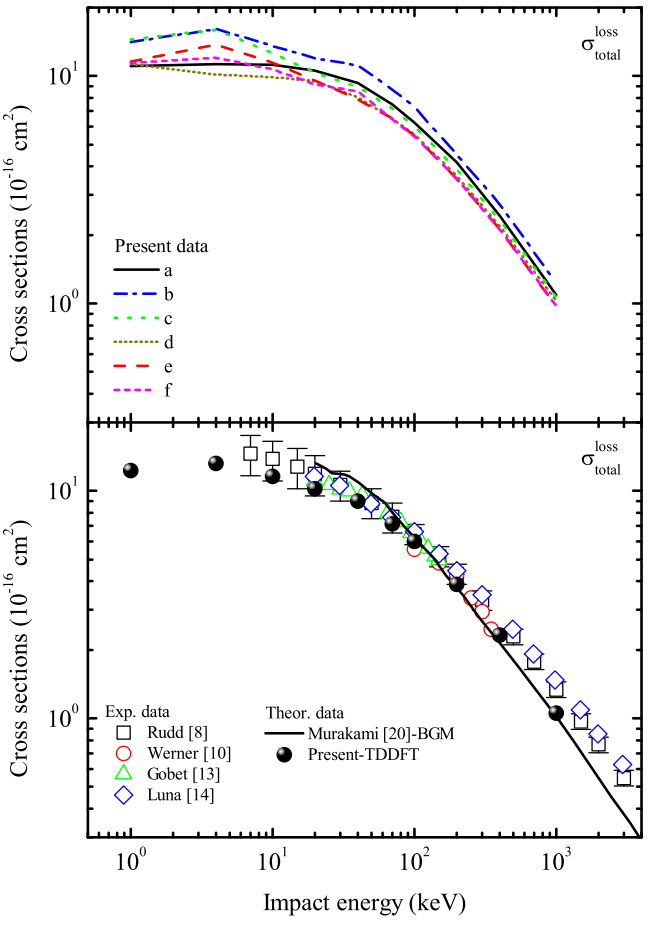

FIG. 6. Top: Present cross sections of electron capture under the collision configurations in Figs. 1(a)–1(f). Bottom: Present total electron loss cross sections ($\sigma_{\rm total}^{\rm loss}$; filled circles) as a function of the incident energies. Other theory, line; experiments, open symbols.

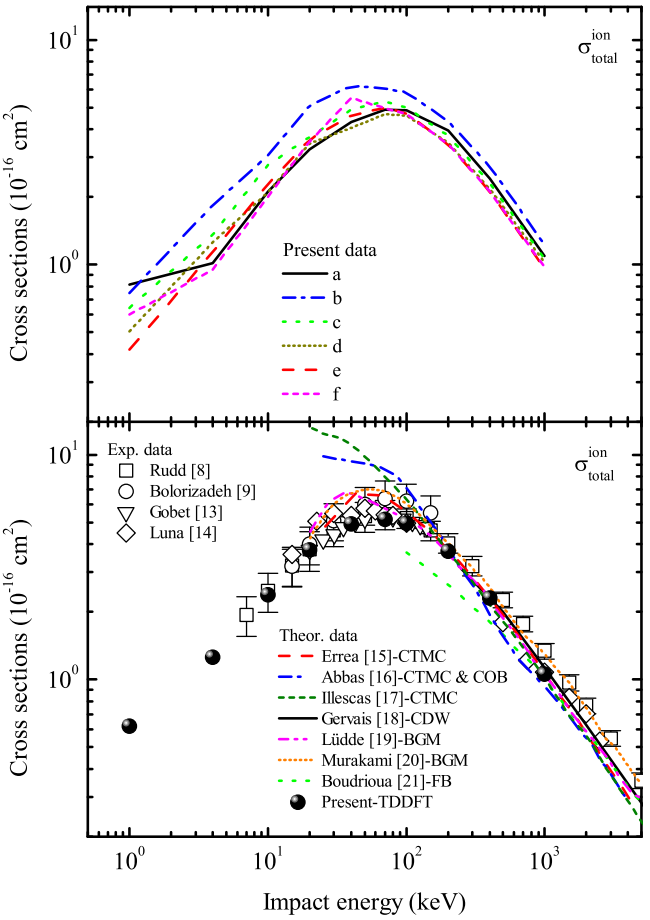

FIG. 7. Top: Present cross sections of electron ionization under the collision configurations in Figs. 1(a)–1(f). Bottom: Present total cross sections of electron ionization (σ^{ion}_{total}; filled circles) as a function of the impact energies. Other theories, lines; experiments, open symbols.

well with our present calculations for energies higher than 100 keV. In the present calculations, the atoms are represented by a pseudopotential, consequently the *K*-shell electrons of the oxygen atom in the water molecule cannot participate in the electron loss contribution, especially at higher incident energies where inner-shell electron loss processes become more important. This explains the divergence between the present calculations and the available measurements at incident energies higher than 400 keV. And further experiments are needed to accurately determine the electron loss cross sections in a higher energy range.

The total ionization cross sections are calculated approximately using Eq. (13) and compared with the available experimental data [8,9,13,14] and theoretical data [15–21], as shown in Fig. 7. The present results agree well with all the experimental data over a wide energy range, from 10 to 1000 keV. The total ionization cross sections approach a maximum at an incident energy of around 50–70 keV. And for lower and higher incident energies, the ionization cross sections decrease rapidly, which indicates that the energy range 50–70 keV is the dominating energy "window" for the ionization process of a water molecule colliding with a proton.

TABLE I. Present total cross sections of electron capture, electron loss, and ionization for H^+-H_2O collisions.

Impact energy	Cross section (10^{-16} cm^2)		
E (keV)	σ^{cap}_{total}	σ^{loss}_{total}	σ^{ion}_{total}
1	11.69677	12.31836	0.62159
4	11.96275	13.22139	1.25864
10	9.19756	11.58490	2.38734
20	6.41809	10.18646	3.76837
40	4.06680	8.99881	4.93201
70	1.99456	7.14160	5.14704
100	1.04787	5.99290	4.94503
200	0.15459	3.88175	3.72716
400	0.01316	2.32066	2.30751
1000	0.00041	1.05801	1.05760

The present calculations also agree well with the classical trajectory Monte Carlo (CTMC) and BGM calculations of Errea [15], Lüdde [19], and Murakami [20] for incident energies higher than 20 keV. The classical trajectory Monte Carlo (CTMC) calculations of Illescas [17] and Abbas [16] agree with other experimental and theoretical data for incident energies higher than about 150 keV. For incident energies higher than 1000 keV, the present calculations converge well to the first Born (FB) calculation of Boudrioua [21], with discrepancies of less than 0.1%. It is known that the perturbative first Born (FB) approximation method usually becomes reliable when the incident energies become higher than tens of the ionization energy of the target. Note that the present TDDFT calculations are the only ones down to an incident energy of as low as 1 keV. The present cross sections of electron capture, electron loss, and ionization are listed in Table I for convenience of comparison.

IV. SUMMARY

The technique of time-dependent density-functional theory combined with the molecular dynamics method has been extended to treatment of ion-molecule collisions, which self-consistently couples the quantum description of electrons and the classical description of ionic cores. The electron exchange and correlation effects in the collisions are reasonably taken into account using the LDA. Based on the real-time and real-space method, the coordinate space translation technique allows one to focus on the region surrounding the target or projectile to extract the stationary probabilities needed. The validity of the present method is demonstrated in the study of H^+-H_2O collisions. Significant orientation effects of the target molecule are observed in the electron capture and electron loss processes, especially for low-energy collisions. For the total electron capture, electron loss, and ionization cross sections, good agreement has been achieved between the present calculations and the available measurements and calculations over the wide energy range of 1–1000 keV. In ion-atom and ion-molecule collisions, the electron capture and ionization processes occur mainly through mutual interactions between the incident ion and target ionic cores and the active electrons of the atom or molecule. For incident energies of

less than a few keV, electron capture dominates the collision processes and usually reaches its maximum when the velocity of the incident ion becomes comparable to the electron orbital velocity of the target. While ionization becomes more dominant at higher incident energies, it usually reaches its maximum when the incident energy increases to several times the ionization energy of the target. In the present simulation, reliable pseudopotentials were employed to treat the interaction between active electrons and ionic cores, and the Ehrenfest method was used to couple electronic and ionic motions self-consistently at each evolution time step, which has been demonstrated to work well for collisions in the energy range 1–1000 keV. The present method is ready to be applied to the treatment of ions colliding with other multiatom molecules.

ACKNOWLEDGMENTS

This work was supported by the National Basic Research program of China (Grant No. 2013CB922200), the National Natural Science Foundation of China (Grants No. 11474032, No. 11474033, No. 11204017, No. 11474020, and No. 11374033), and the Project funded by China Postdoctoral Science Foundation (Grant No. 2015M570977).

[1] C. L. Zhang, X. H. Hong, F. Wang, Y. Wu, and J. G. Wang, Phys. Rev. A **87**, 032711 (2013).
[2] T. E. Cravens, Science **296**, 1042 (2002).
[3] H. Nikjoo, S. Uehara, D. Emfletzoglou, and A. Brahme, New J. Phys. **10**, 075006 (2008).
[4] E. S. Chambers, Phys. Rev. **139**, A1068 (1965).
[5] L. H. Toburen, M. Y. Nakai, and R. A. Langley, Phys. Rev. **171**, 114 (1968).
[6] K. H. Berkner, R. V. Pyle, and J. W. Stearns, Nucl. Fusion **10**, 145 (1970).
[7] R. Dagnac, D. Blanc, and D. Molina, J. Phys. B **3**, 1239 (1970).
[8] M. E. Rudd, T. V. Goffe, R. D. DuBois, and L. H. Toburen, Phys. Rev. A **31**, 492 (1985).
[9] M. A. Bolorizadeh and M. E. Rudd, Phys. Rev. A **33**, 888 (1986).
[10] U. Werner, K. Beckord, J. Becker, and H. O. Lutz, Phys. Rev. Lett. **74**, 1962 (1995).
[11] B. G. Lindsay, D. R. Sieglaff, K. A. Smith, and R. F. Stebbings, Phys. Rev. A **55**, 3945 (1997).
[12] J. B. Greenwood, A. Chutjian, and S. J. Smith, Astrophys. J. **529**, 605 (2000).
[13] F. Gobet, S. Eden, B. Coupier, J. Tabet, B. Farizon, M. Farizon, M. J. Gaillard, M. Carré, S. Ouaskit, T. D. Märk, and P. Scheier, Phys. Rev. A **70**, 062716 (2004).
[14] H. Luna, A. L. F. de Barros, J. A. Wyer, S. W. J. Scully, J. Lecointre, P. M. Y. Garcia, G. M. Sigaud, A. C. F. Santos, V. Senthil, M. B. Shah, C. J. Latimer, and E. C. Montenegro, Phys. Rev. A **75**, 042711 (2007).
[15] L. F. Errea, C. Illescas, L. Méndez, B. Pons, I. Rabadán, and A. Riera, Phys. Rev. A **76**, 040701 (2007).
[16] I. Abbas, C. Champion, B. Zarour, B. Lasri, and J. Hanssen, Phys. Med. Biol. **53**, N41 (2008).
[17] C. Illescas, L. F. Errea, L. Méndez, B. Pons, I. Rabadán, and A. Riera, Phys. Rev. A **83**, 052704 (2011).
[18] B. Gervais, M. Beuve, G. H. Olivera, and M. E. Galassi, Radiat. Phys. Chem. **75**, 493 (2006).
[19] H. J. Lüdde, T. Spranger, M. Horbatsch, and T. Kirchner, Phys. Rev. A **80**, 060702 (2009).
[20] M. Murakami, T. Kirchner, M. Horbatsch, and H. J. Lüdde, Phys. Rev. A **85**, 052704 (2012).
[21] O. Boudrioua, C. Champion, C. Dal Cappello, and Y. V. Popov, Phys. Rev. A **75**, 022720 (2007).
[22] S. Mada, K. N. Hida, M. Kimura, L. Pichl, H. P. Liebermann, Y. Li, and R. J. Buenker, Phys. Rev. A **75**, 022706 (2007).
[23] P. M. M. Gabás, L. F. Errea, L. Méndez, and I. Rabadán, Phys. Rev. A **85**, 012702 (2012).
[24] F. Wang, X. H. Hong, J. Wang, and K. S. Kim, J. Chem. Phys. **134**, 154308 (2011).
[25] F. Wang, X. C. Xu, X. H. Hong, J. Wang, and B. C. Gou, Phys. Lett. A **375**, 3290 (2011); F. Wang, X. H. Hong, J. Wang, B. C. Gou, and J. G. Wang, *ibid.* **376**, 469 (2012).
[26] E. K. U. Gross, J. F. Dobson, and M. Petersilka, *Density Functional Theory of Time-Dependent Phenomena* (Springer-Verlag, Berlin, 1996).
[27] E. Runge and E. K. U. Gross, Phys. Rev. Lett. **52**, 997 (1984).
[28] J. R. Chelikowsky, N. Troullier, K. Wu, and Y. Saad, Phys. Rev. B **50**, 11355 (1994).
[29] N. Troullier and J. L. Martins, Phys. Rev. B **43**, 1993 (1991).
[30] F. Calvayrac, P. G. Reinhard, E. Suraud, and C. A. Ullrich, Phys. Rep. **337**, 493 (2000).
[31] P. G. Reinhard and E. Suraud, *Introduction to Cluster Dynamics* (Wiley, New York, 2003).
[32] E. K. U. Gross, C. A. Ullrich, and U. J. Gossmann, *Density Functional Theory* (Plenum Press, New York, 1994).
[33] R. Nagano, K. Yabana, T. Tazawa, and Y. Abe, J. Phys. B **32**, L65 (1999).
[34] Z. P. Wang, P. M. Dinh, P.-G. Reinhard, E. Suraud, G. Bruny, C. Montano, S. Feil, S. Eden, H. Abdoul-Carime, B. Farizon, M. Farizon, S. Ouaskit, and T. D. Mark, Int. J. Mass Spectrom. **285**, 143 (2009); Z. P. Wang, P. M. Dinh, P.-G. Reinhard, E. Suraud, and F. S. Zhang, Int. J. Quantum Chem. **111**, 480 (2011).
[35] A. Castro, M. Isla, J. I. Martlnez, and J. A. Alonso, Chem. Phys. **399**, 130 (2012).
[36] C. Z. Gao, J. Wang, and F. S. Zhang, Chem. Phys. **410**, 9 (2013); J. Wang, C. Z. Gao, and F. S. Zhang, Chem. Phys. Lett. **556**, 256 (2013); C. Z. Gao, J. Wang, F. Wang, and F. S. Zhang, J. Chem. Phys. **140**, 054308 (2014).
[37] A. Castro, M. A. L. Marques, and A. Rubio, J. Chem. Phys. **121**, 3425 (2004).
[38] P. Ehrenfest, Z. Phys. **45**, 455 (1927); J. B. Delos, W. B. Thorson, and S. K. Knudsen, Phys. Rev. A **6**, 709 (1972); D. A. Micha, J. Chem. Phys. **78**, 7138 (1983).
[39] O. Sugino and Y. Miyamoto, Phys. Rev. B **59**, 2579 (1999).
[40] L. Verlet, Phys. Rev. **159**, 98 (1967).
[41] Dz. Belkić, I. Mancev, and J. Hanssen, Rev. Mod. Phys. **80**, 249 (2008).
[42] Dz. Belkić, J. Math. Chem. **47**, 1366 (2010).
[43] Dz. Belkić, J. Math. Chem. **47**, 1420 (2010).

[44] H. J. Lüdde and R. M. Dreizler, J. Phys. B **16**, 3973 (1983).
[45] M. A. L. Marques, A. Castro, G. F. Bertsch, and A. Rubio, Comput. Phys. Commun. **151**, 60 (2003); A. Castro, H. Appel, M. Oliveira, C. A. Rozzi, X. Andrade, F. Lorenzen, M. A. L. Marques, E. K. U. Gross, and A. Rubio, Phys. Status Solidi B **243**, 2465 (2006).
[46] J. G. Muga, J. P. Palao, B. Navarro, and I. L. Egusquiza, Phys. Rep. **395**, 357 (2004).
[47] R. Kosloff and D. Kosloff, J. Comput. Phys. **63**, 363 (1986).
[48] F. He, C. Ruiz, and A. Becker, Phys. Rev. A **75**, 053407 (2007).
[49] C. A. Ullrich, P. G. Reinhard, and E. Suraud, Phys. Rev. A **57**, 1938 (1998).
[50] F. Calvayrac, P. G. Reinhard, and E. Suraud, Ann. Phys. **255**, 125 (1997); J. Phys. B **31**, 5023 (1998).
[51] Dz. Belkić, *Principle of Quantum Scattering Theory* (Institute of Physics Publishing, Bristol, UK, 2004).